J. Fluid Mech. (2011), *vol.* 677, *pp.* 483–502. © Cambridge University Press 2011
doi:10.1017/jfm.2011.96

Numerical study of flow fields in an airway closure model

C.-F. TAI[1]†, S. BIAN[1], D. HALPERN[2], Y. ZHENG[1], M. FILOCHE[3] AND J. B. GROTBERG[1]

[1]Department of Biomedical Engineering, University of Michigan, Ann Arbor, MI 48109, USA
[2]Department of Mathematics, University of Alabama, Tuscaloosa, AL 35487, USA
[3]Physique de la Matière Condensée, Ecole Polytechnique, CNRS, 91128 Palaiseau, France

(Received 1 April 2010; revised 11 February 2011; accepted 20 February 2011; first published online 8 April 2011)

The liquid lining in small human airways can become unstable and form liquid plugs that close off the airways. Direct numerical simulations are carried out on an airway model to study this airway instability and the flow-induced stresses on the airway walls. The equations governing the fluid motion and the interfacial boundary conditions are solved using the finite-volume method coupled with the sharp interface method for the free surface. The dynamics of the closure process is simulated for a viscous Newtonian film with constant surface tension and a passive core gas phase. In addition, a special case is examined that considers the core dynamics so that comparisons can be made with the experiments of Bian *et al.* (*J. Fluid Mech.*, vol. 647, 2010, p. 391). The computed flow fields and stress distributions are consistent with the experimental findings. Within the short time span of the closure process, there are large fluctuations in the wall shear stress. Furthermore, dramatic velocity changes in the film during closure indicate a steep normal stress gradient on the airway wall. The computational results show that the wall shear stress, normal stress and their gradients during closure can be high enough to injure airway epithelial cells.

Key words: multiphase flow

1. Introduction

The lung's airways are coated with an annular liquid film. When the ratio of the liquid film thickness to the airway radius is sufficiently large, a disturbance in the liquid lining can amplify and a plug can be formed that closes off the airway. The lung volume at which this occurs is known as the 'closing volume'. In normal gravity, closure usually occurs in the lower airways of an upright human, since the airway radius is compressed from the lung's weight. In a microgravity environment, the airway closure would tend to be more homogeneous since the lung weight is not compressing the lower lung. The formation of the plug due to airway closure might limit gas exchange if the closing volume is large. Furthermore, the formation of the plug can lead to the complete collapse of the airway due to the axial draining of ambient film fluid into the plug (Macklem, Proctor & Hogg 1970; Greaves, Hildebrandt & Hoppin 1986). Airway closure usually happens in the small airways near the end of expiration, often accompanied with hypersecretion or/and surfactant

† Email address for correspondence: petertai@umich.edu

https://doi.org/10.1017/jfm.2011.96 Published online by Cambridge University Press

deficiency in the airway in a variety of lung diseases, such as chronic obstructive pulmonary disease (COPD; Guerin *et al.* 1997), cystic fibrosis (Griese *et al.* 2004), acute respiratory distress syndrome (ARDS; Baker *et al.* 1999), pneumonia (Gunther *et al.* 1996), bronchiolitis (Dargaville, South & McDougall 1996) and asthma (t Veen *et al.* 2000). During inhalation, the liquid plug in an airway propagates distally. It can eventually rupture as the airway reopens. The transient pressure wave generated by the abrupt reopening might be detected by a stethoscope as a crackle sound (Piirila & Sovijarvi 1995; Rasanen & Gavriely 2005).

Modelling work by Halpern & Grotberg (1992) has shown that several forces could contribute to airway closure, such as surface tension instability and wall compliance. Experiments in a capillary tube were conducted by Cassidy *et al.* (1999) to examine surfactant effects on airway closure. They measured the relationship between the film thickness at various infusion flow rates of the core fluid, the instability growth rate and the closure time. It was found that the surfactant decreased the growth rate by 20 % and increased the closure time as well as the critical film thickness. A review of the mechanics of airway closure is given by Heil, Hazel & Smith (2008), who discussed both the purely fluid-mechanical 'film collapse' and the coupled, fluid-elastic 'compliant collapse' mechanism.

Flow-induced stresses on the airway epithelial cells might lead to severe cell injury. Gaver and colleagues (Bilek, Dee & Gaver 2003; Kay *et al.* 2004) experimentally investigated cell injury during airway reopening by using an air finger moving through a liquid-filled, parallel-plate chamber lined with cultured pulmonary epithelial cells. Significant cell damage was found due to the mechanical stress induced by the bubble propagation. It was also revealed that pulmonary surfactant relieves the flow-induced stresses and, consequently, decreases cell damage. Experimental studies (Muscedere *et al.* 1994; Taskar *et al.* 1997) on excised lungs and *in vivo* animal models have shown that severe tissue damage was found in surfactant-deficient lungs due to the repetitive airway reopening. Ghadiali & Gaver (2008) gave a review of the effects of surface tension forces on the mechanics of airway reopening and epithelial cell injury. Huh *et al.* (2007) illustrated that exposure of primary human airway epithelial cells to liquid plug propagation and rupture led to significant cell injury. Numerical simulations of liquid plug propagation in a rigid channel (Fujioka & Grotberg 2004, 2005; Fujioka, Takayama & Grotberg 2008) confirmed that sharp peaks in wall stresses and stress gradients were present in the transition region of the plug during plug propagation. In addition, experimental and numerical studies of plug propagation in flexible microchannels (Zheng *et al.* 2009) predicted a higher level of wall stresses and stress gradients along a highly deformable wall as compared to a rigid channel wall.

Although it is well recognized that airway reopening can induce epithelial damage from fluid forces, the same cannot be said about airway closure. Dramatic changes in flow velocity and pressure in the film fluid during the dynamic process of airway closure can lead to high stress and stress gradients that might damage the epithelial cells on the airway. The capillary instability in the liquid lining of a rigid tube was measured and simulated by Cassidy *et al.* (1999). Recently, Bian *et al.* (2010) measured the velocity field in the film fluid. Quantifying the velocity field is critical to understanding the flow-induced stresses on the airway epithelial cells during airway closure and, therefore, is of great importance to sustaining the normal functions of the lung and preventing deleterious fluid-induced stresses.

Over the last few decades, there have been several theoretical models of airway closure (Johnson *et al.* 1991; Halpern & Grotberg 1992, 1993, 2003; Heil 1999;

https://doi.org/10.1017/jfm.2011.96 Published online by Cambridge University Press

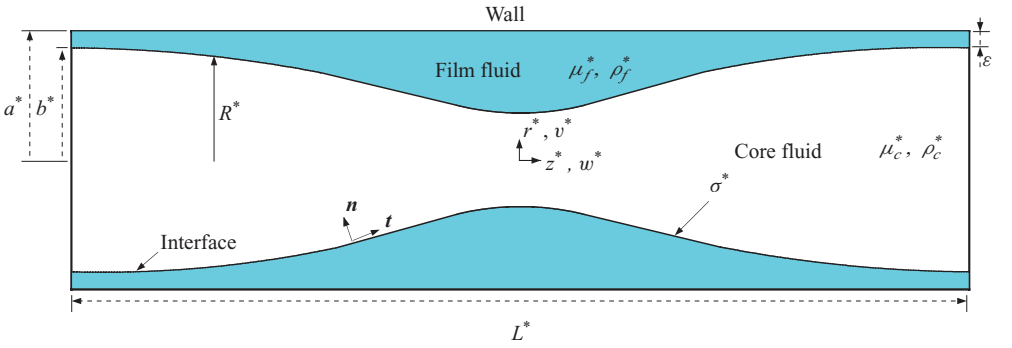


FIGURE 1. Schematic diagram of the problem: $r^* = a^*$ is the airway radius, $r^* = b^*$ is the undisturbed location of the interface, and $r = R^*$ is the perturbed location of the interface.

White & Heil 2005). Some are based on lubrication theory and assume that the film is thin and inertia is not important. These have been used to estimate the critical film thickness for closure and the closure time. However, the lubrication theory models break down when the film is no longer thin and, therefore, are not expected to accurately describe the flow field and wall stresses when closure occurs. Campana, Di Paolo & Saita (2004) applied two-dimensional (2-D) free-surface flow model to analyse numerically the instability of a film lining a rigid capillary tube. Campana & Saita (2006) studied numerically the influence of surfactant solubility on the growth rate of the film instability in capillary tubes. Heil (1999) calculated the non-axisymmetric wall deformations during airway closure and demonstrated that non-axisymmetric airway collapse allows plug formation with far less fluid than that required in an axisymmetric collapse. White & Heil (2005) demonstrated that the occurrence of the non-axisymmetric instability may cause the formation of a liquid plug, although the airway system is evolving axisymmetrically towards a non-closing equilibrium state due to insufficient film fluid volume.

In the current study, a direct numerical simulation (DNS) approach is adopted to simulate this airway closure problem. In § 2, the governing equations describing the dynamics of a liquid layer coating the inner surface of a rigid tube with a circular cross-section are given. In this model, the gas phase is assumed to be quiescent and the surface tension to be constant. The description of the sharp interface method (SIM) used to solve the fluid flow (Ye *et al.* 2004; Tai & Shyy 2005) appears in § 3. The stress balance condition is used to determine the shape and movement of the interface at each time step. The primary flow variables and the location of the interface are computed as well as the flow-induced normal and shear stresses, which are then compared with the experimental results of Bian *et al.* (2010). Results and discussion are given in § 4, and conclusions appear in § 5.

2. Problem description and governing equations

2.1. *Problem description*

Our model consists of a core fluid with viscosity μ_c^* and density ρ_c^* representing the gas phase, which is surrounded by a thin liquid film with viscosity μ_f^* and density ρ_f^* that coats the inner surface of a cylindrical rigid tube of radius a^* and length L^*, as shown in figure 1. Here, and below, the subscript 'f' stands for the film and 'c' for the core liquid.

https://doi.org/10.1017/jfm.2011.96 Published online by Cambridge University Press

Initially, the film has a uniform thickness $a^* - b^*$ and there is no motion in both fluid layers. To investigate the stability of this system, R^*, the radial location of the interface, is perturbed by a single mode with amplitude that is 1 % of the initial film thickness,

$$R^* = b^* - 0.01 \times \left(\frac{a^* - b^*}{a^*}\right) \cos(2\pi z^*/L^*), \tag{2.1}$$

where z^* is the distance along the axis of the tube. Figure 1 also shows $\boldsymbol{n}$, the unit normal vector at the interface pointing towards the gas phase. In the analysis presented below the surface tension σ^* at the interface is assumed to be constant.

2.2. *Governing equations for the perturbed film flow*

The equations governing the fluid motion in the liquids after the interface has been perturbed from its uniform state are the following continuity and the Navier–Stokes equations:

$$\left.\begin{aligned} \nabla^* \cdot \boldsymbol{u}_f^* = 0, \quad \rho_f^* \left(\frac{\partial \boldsymbol{u}_f^*}{\partial t^*} + \boldsymbol{u}_f^* \cdot \nabla^* \boldsymbol{u}_f^*\right) = -\nabla^* p_f^* + \mu_f^* \nabla^{*2} \boldsymbol{u}_f^*, \\ \nabla^* \cdot \boldsymbol{u}_c^* = 0, \quad \rho_c^* \left(\frac{\partial \boldsymbol{u}_c^*}{\partial t^*} + \boldsymbol{u}_c^* \cdot \nabla^* \boldsymbol{u}_c^*\right) = -\nabla^* p_c^* + \mu_c^* \nabla^{*2} \boldsymbol{u}_c^*, \end{aligned}\right\} \tag{2.2}$$

where t^* is time, $\boldsymbol{u}_i^* = (w_i^*, v_i^*)$ is the velocity vector, and p_i^* is the pressure. At the interface, $r^* = R^*(z^*, t^*)$, there is a jump in the normal stress balanced by surface tension:

$$(p_f^* - p_c^*)\boldsymbol{n} = -\sigma^* \kappa^* \boldsymbol{n} + (\boldsymbol{\tau}_f^* \cdot \boldsymbol{n}) - (\boldsymbol{\tau}_c^* \cdot \boldsymbol{n}), \tag{2.3}$$

where $\boldsymbol{\tau}_i^* = \mu_i(\nabla^* \boldsymbol{u}_i^* + (\nabla^* \boldsymbol{u}_i^*)^{\mathrm{T}})$ is the viscous stress tensor and κ^* is the curvature. At the tube wall, $r^* = a^*$, no-slip and no-penetration conditions are applied:

$$\boldsymbol{u}^* = 0. \tag{2.4}$$

Periodic boundary conditions are applied at the tube ends $z^* = -L^*/2$ and $z^* = L^*/2$:

$$\boldsymbol{u}_i^*|_{z^* = -L^*/2} = \boldsymbol{u}_i^*|_{z^* = L^*/2}. \tag{2.5}$$

The non-dimensionalization of the equations and boundary conditions is similar to that used in Halpern & Grotberg (1992). The characteristic length and time scales are respectively

$$L_c = a^*, \quad T = \frac{\mu_f^* a^*}{\varepsilon^3 \sigma^*}, \tag{2.6}$$

where ε is the dimensionless initial film thickness:

$$\varepsilon = \frac{a^* - b^*}{a^*}. \tag{2.7}$$

The following dimensionless (unstarred) variables are introduced:

$$r = \frac{r^*}{L_c}, \quad z = \frac{z^*}{L_c}, \quad t = \frac{t^*}{T}, \quad \boldsymbol{u}_i = \frac{\boldsymbol{u}_i^*}{(L_c/T)}, \quad p_i = \frac{p_i^*}{(\varepsilon \sigma^*/a^*)}. \tag{2.8}$$

https://doi.org/10.1017/jfm.2011.96 Published online by Cambridge University Press

Consequently, the dimensionless versions of equations (2.2) and (2.3) are:

$$\left.\begin{aligned} &\nabla\cdot\boldsymbol{u}_f = 0, \quad \left(\frac{\partial \boldsymbol{u}_f}{\partial t} + \boldsymbol{u}_f\cdot\nabla\boldsymbol{u}_f\right) = -\frac{1}{\varepsilon^2 Re}\nabla p_f + \frac{1}{Re}\nabla^2\boldsymbol{u}_f,\\ &\nabla\cdot\boldsymbol{u}_c = 0, \quad \frac{\rho_c^*}{\rho_f^*}\left(\frac{\partial \boldsymbol{u}_c}{\partial t} + \boldsymbol{u}_c\cdot\nabla\boldsymbol{u}_c\right) = -\frac{1}{\varepsilon^2 Re}\nabla p_c + \frac{\mu_c^*}{\mu_f^*}\frac{1}{Re}\nabla^2\boldsymbol{u}_c,\\ &(p_f - p_c)\cdot\boldsymbol{n} = -\frac{\kappa}{\varepsilon}\boldsymbol{n} + \frac{1}{\varepsilon^2}(\boldsymbol{\tau}_f\cdot\boldsymbol{n}) - \frac{\mu_c^*}{\mu_f^*}\frac{1}{\varepsilon^2}(\boldsymbol{\tau}_c\cdot\boldsymbol{n}), \end{aligned}\right\} \tag{2.9}$$

where Re is the Reynolds number

$$Re = \frac{\rho_f^* a^* \varepsilon^3 \sigma^*}{\mu_f^{*2}}. \tag{2.10}$$

When the core fluid is a gas with $\mu_c^* = \mu_g^*$, the dynamics of the core can be neglected and the pressure can be assumed to be constant (Hammond 1983). The initial pressure in the liquid film is set as zero and therefore the pressure in the gas core is $p_c = \kappa/\varepsilon$, where $\kappa = 1/R_0$ and $R_0 = 1-\varepsilon$ in order to balance the surface tension. When the gas core is assumed to be passive, the governing equations and the interfacial stress condition can be simplified as

$$\left.\begin{aligned} &\nabla\cdot\boldsymbol{u}_f = 0, \quad \left(\frac{\partial \boldsymbol{u}_f}{\partial t} + \boldsymbol{u}_f\cdot\nabla\boldsymbol{u}_f\right) = -\frac{1}{\varepsilon^2 Re}\nabla p_f + \frac{1}{Re}\nabla^2\boldsymbol{u}_f,\\ &(p_f - p_c)\cdot\boldsymbol{n} = -\frac{\kappa}{\varepsilon}\boldsymbol{n} + \frac{1}{\varepsilon^2}(\boldsymbol{\tau}_f\cdot\boldsymbol{n}). \end{aligned}\right\} \tag{2.11}$$

The non-dimensionalization introduced in (2.8) is appropriate during the initial stages of the instability. We chose a capillary pressure scale using the normal-stress boundary condition, and a viscous capillary scale for the velocity by balancing the pressure and viscous terms in the axial momentum equation. The time scale was obtained from the kinematic boundary condition. These scalings have been used by lubrication theory models that can accurately capture the onset of the closure event but not the ultimate pinch-off. It should be pointed out that the exact equations and boundary conditions that are solved using the DNS approach could have been non-dimensionalized using a set of scales that is relevant during the pinch-off (closure) event when inertia becomes important. Numerically, this is not important since none of the terms in the Navier–Stokes equations and the boundary conditions are being neglected. Some post-processing can be done to investigate what happens near the closure event.

3. Numerical method

3.1. *The sharp-interface method*

A DNS technique is adopted to directly simulate the moving interfacial problem in this study. In the earlier development of computational multiphase flow, some researchers adopted the curvilinear grid system (Ryskin & Leal 1984). This approach is simple but not easy to apply. In order to describe the deformation of an interface between different phases, a very powerful grid generation is required and, further, the grid has to be updated frequently to obtain the convergent solution and therefore it is computationally intensive. Also, this approach is not good if the interface undergoes a large deformation since the mesh can be greatly distorted, making it difficult to obtain an accurate solution.

https://doi.org/10.1017/jfm.2011.96 Published online by Cambridge University Press

In recent multiphase computations, several Cartesian grid methods have been introduced such as the sharp-interface method (Tai & Shyy 2005), the immersed-boundary method (IBM; Peskin 1977), the volume-of-fluid method (VOF; Hirt & Nichols 1981) and the level-set method (LSM; Osher & Fedkiw 2003). On the basis of the computational framework, sharp-interface and immersed-boundary methods are classified under the mixed Eulerian–Lagrangian category and level-set and volume-of-fluid methods are in the Eulerian category (Shyy 1994).

In the airway closure problem, high resolution of solutions (primary variables) near the interface is necessary. The initial perturbation and the induced initial interfacial velocity are both very small, with the order of magnitude of the initial interfacial velocity being approximately 10^{-5}. In order to accurately catch this small quantity, the SIM is selected in this study to avoid the error that can come from the poor resolution of primary variables near the interface.

In the SIM, the Cartesian grid is designed as a background mesh, and explicit interfaces are used to describe the shapes of the objects on the background grid. The interfacial dynamics associated with the moving/fixed boundaries needs to be considered simultaneously. In the mixed Eulerian–Lagrangian approach, the interface is constructed by a sequence of marker points. With these marker points, the shape and location of the interface are determined by designated interpolation procedures, while the overall fluid flow is computed on the fixed Cartesian grid. In the SIM, the interface is treated explicitly with zero thickness, in accordance with the continuum mechanics model. The primary variables at the interface are computed via the interfacial conditions. The SIM defines the relations between the background grid and the interface. The key elements of the SIM are listed in the next three subsections.

3.1.1. *The fixed Cartesian grid and fractional step method*

The computational framework is built on an Eulerian Cartesian grid to facilitate the field equation computation. For each phase domain, a finite-volume, fractional step method (Ferziger & Peric 1996) is used to numerically integrate the governing equations in that phase.

3.1.2. *The Lagrangian moving sharp-interface algorithm*

Within the fixed-grid framework, the sharp interface is identified and tracked by separate marker points to form the Lagrangian portion of this method. The interface can be either a fixed solid boundary (such as the tube wall) or a moving phase boundary (such as the gas–liquid interface). With a moving phase boundary, the motion of the interface is tracked through the translation of the marker points over the stationary Cartesian grid. These marker points are connected by quadratic curve fitting, which is employed to capture the deformation and movement of the sharp interface. The overall solution is obtained by matching the mass and momentum fluxes from both phases at the sharp interface. Figure 2 gives an illustration of a moving interface. Initially, a maker point, M_n^0, is located on the interface. The location of the interface (that is the marker points) is determined using an iterative process. At each time step, the maximum number of iterations is assigned to be 200. The superscript m represents the iteration counter, with $m = 0$ denoting the initial condition at a particular time step. The subscript n represents the current time. The governing equations in each phase are solved and the intermediate primary variables are obtained. These intermediate primary variables are used to compute the residual of the stress balance equation, Π_n^m. The displacement of the interface is assumed to be proportional to this residual. The intermediate displacement, $\Delta \boldsymbol{X}_n^m$, location, $\boldsymbol{X}_n^m$,

https://doi.org/10.1017/jfm.2011.96 Published online by Cambridge University Press

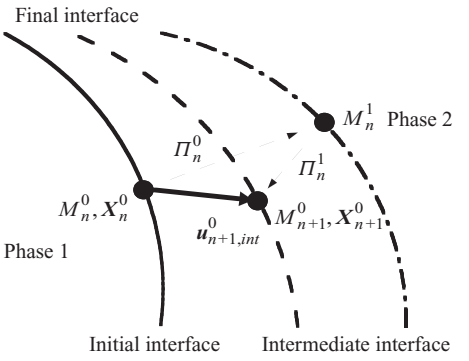


FIGURE 2. Adjustment of the interface in SIM.

and interfacial velocity, $\boldsymbol{u}_{n,int}^m$, are computed as follows:

$$\left.\begin{aligned} \Delta \boldsymbol{X}_n^m &= \Pi_n^m \beta \boldsymbol{n}, \\ \boldsymbol{X}_n^m &= \boldsymbol{X}_n^{m-1} + \Delta \boldsymbol{X}_n^m, \\ \boldsymbol{u}_{n,int}^m &= \frac{\boldsymbol{X}_n^m - \boldsymbol{X}_n^0}{\Delta t}, \end{aligned}\right\} \tag{3.1}$$

where β is a relaxation factor which is of the order of 10^{-4} in this study, Π_n^m is the residual of the interfacial condition and $\boldsymbol{X}_n^0$ is the initial position at the current time step. This displacement pushes M_n^0 to M_n^1 on the intermediate interface. The governing equations are solved again to find another residual of the stress balance condition, and the shape of the interface is adjusted again based on this new residual. These operations are repeated until finally the residual of the interfacial condition is less than 10^{-3} and the residual of the solver of the governing equations is less than 10^{-6}. Once both conditions are satisfied, the interfacial velocity for the next time step can be obtained,

$$\boldsymbol{u}_{n+1,int}^0 = \frac{\boldsymbol{X}_{n+1}^0 - \boldsymbol{X}_n^0}{\Delta t}, \quad \boldsymbol{X}_{n+1}^0 = \boldsymbol{X}_n^m, \tag{3.2}$$

where $\boldsymbol{X}_{n+1}^0$ is the location of the marker point at the next time step.

3.1.3. *The cut-cell scheme*

A cut-cell scheme developed in Ye *et al.* (2004) is used to handle irregular intersections between an interface and the Cartesian grid line. Some cells containing the interface are cut and form non-rectangular cut cells. Special methods are needed to treat these cut cells. In the interface region, the grid is recombined to form irregularly shaped cells by the cut-cell scheme. Consistent interpolation formulae are chosen for estimation of the fluxes along any of the cell surfaces. In this research, the shapes of the cut cells can be triangles, trapezoids and pentagons. Figure 3 is an example of the grid system featured in SIM. The entire Cartesian grid system becomes a mixed-type grid system at the interface constructed by rectangular cells not involved with the interface and cut cells containing the interface.

Details related to the fractional step method within the finite-volume framework, the cut-cell scheme, the moving interface algorithm and the interfacial tracking can be found elsewhere (Ye *et al.* 2004). The current method is globally second-order accurate. For all the numerical simulations given in the next section, a 80×540 grid is used. Each case takes approximately 120 CPU h on an Intel® E5430, 2.66 GHz CPU.

https://doi.org/10.1017/jfm.2011.96 Published online by Cambridge University Press

Parameters	Values
ε	0.19, 0.23, 0.27
L	6.8
Re	0.56, 1.0, 1.61

TABLE 1. Values of the dimensionless parameters used in this study.

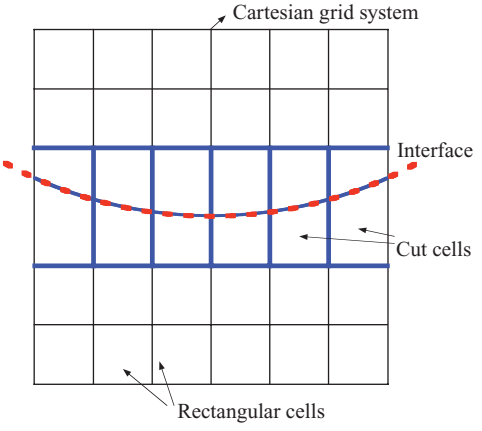


FIGURE 3. The mixed rectangular and cut-cell grid in SIM.

4. Results and discussion

In this study, the following dimensional parameters are selected for the airway closure model:

$$\left.\begin{array}{c} a^* = 0.065\,\text{cm}, \quad L^* = 0.44\,\text{cm}, \quad \rho_f^* = 1.0\,\text{g cm}^{-3}, \quad \sigma^* = 20\,\text{dyn cm}^{-1} \\ \mu_f^* = 0.13\,\text{poise}. \end{array}\right\} \tag{4.1}$$

This set of the dimensional parameters can represent the dimensions of the airway at generation 10 in the adult lung (Crystal 1997). Our chosen value for the viscosity of the liquid is higher than that of water because we assume that the liquid is a mixture of the mucus and serous fluids found in the lung's liquid lining. The chosen value for the surface tension is lower than at an air–water interface since surfactants are present in the lung. However, we have assumed that the surface tension is constant in our model. There are three dimensionless parameters in this study: the dimensionless length of the tube, the initial film thickness and the Reynolds number. In order to compare with the experimental data (Bian *et al.* 2010), the dimensionless length of the tube is assigned as $L = 6.8$. Three initial dimensionless film thicknesses are selected: $\varepsilon = 0.19$, 0.23 and 0.27. The Reynolds number is computed using the above dimensional parameters. Table 1 gives the values of the various dimensionless parameters used in this study.

4.1. *Validation*

First, we compare the current SIM (DNS) results with the results obtained by the lubrication theory model, which is often used to solve thin film problems to ensure that our current numerical approach is reliable. Figure 4 shows comparisons of the dimensionless histories of the maximum interfacial velocity and R_{min} (the minimum distance between the interface and the centreline) between the lubrication

https://doi.org/10.1017/jfm.2011.96 Published online by Cambridge University Press

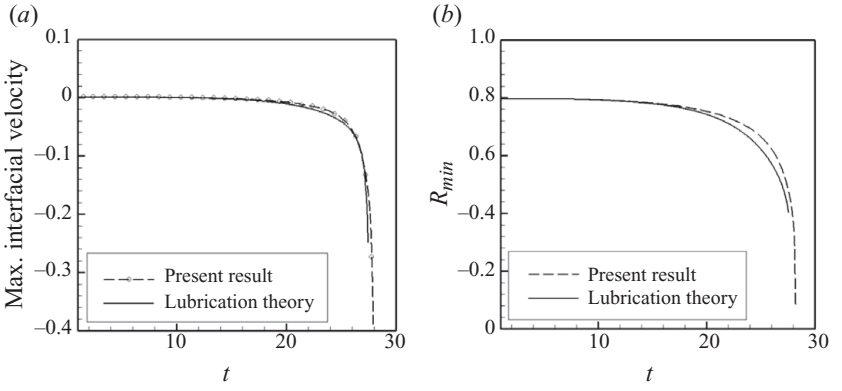


FIGURE 4. Comparison between lubrication theory and present computational results: the time histories of (*a*) maximum interfacial velocity and (*b*) minimum core radius R_{min}.

theory model (Halpern, Fujioka & Grotberg 2010) and the SIM with $L = 9.0$, $\varepsilon = 0.2$ and $Re = 1.0$. Results shown in figure 4 demonstrate good agreement between both approaches until $t = 18$, and an increasing deviation occurs between them after $t = 18$. Note that in the lubrication theory model, inertia is neglected and the pressure is a function of the axial location and time, that is $p = p(z, t)$. When the deformation is small, both assumptions are reasonable but may not be so good when the deformation becomes large, prior to the pinch-off. In figure 4, it can be seen that the interfacial velocity is slightly higher using the lubrication theory model, so that the closure time is slightly shorter. Once the deformation is large enough, the interfacial velocity dramatically increases with time due to the stronger influence of surface tension.

Overall, the comparison at early times is very favourable, which means that just like the lubrication theory model, the SIM is able to accurately capture the initial stages of the instability. Moreover, the SIM is more accurate than the lubrication theory model, when the deformation becomes sufficiently large ($R_{min} < 0.4$) since no special assumptions are made in the SIM.

4.2. *Comparisons between numerical simulations and benchtop experiments*

Next, a special case is considered that takes into account the dynamics of the core fluid, so that we can make comparisons with the experimental results of Bian *et al.* (2010). The density ratio $\rho_f^*/\rho_c^* = 1.05$ and the viscosity ratio $\mu_f^*/\mu_c^* = 100$ are the same as in the experiments. The governing equations in each phase are solved numerically using the method described above. The pressure in the core part is no longer a constant and is adjusted to satisfy the interfacial stress condition. Figure 5(*a*) shows the streamlines in both phases at an instant in time just before closure occurs. The liquids in each phase are pulled and pushed by the interface and form two symmetric vortices.

Figure 5(*b*) shows how the minimum core radius, R_{min}, varies with $(t_c - t)$ for $\varepsilon = 0.23$ and in the numerical simulations with an initial amplitude of 0.01ε. As t approaches t_c, R_{min} decreases to zero at an ever-increasing rate, indicating that the core pinches off at some location along the interface in a singular manner. Although figure 5(*b*) indicates that there is relatively good agreement with regard to the rate of decrease of R_{min}, when R_{min} is small between the two theoretical approaches and the experimental results of Bian *et al.* (2010), there are some important discrepancies that are highlighted next. For example, there is a significant difference in the estimated closure time (scaled by $a^*\mu_f^*/\varepsilon^3\sigma^*$): it is approximately equal to 26 using the lubrication theory model,

https://doi.org/10.1017/jfm.2011.96 Published online by Cambridge University Press

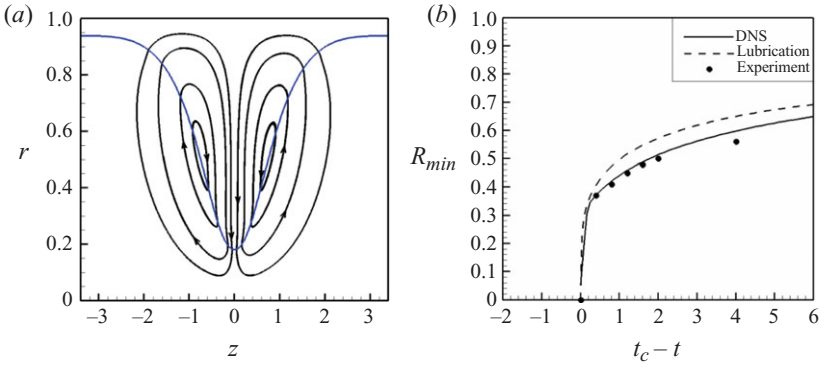


FIGURE 5. (*a*) Streamline plot and (*b*) the comparisons of R_{min} near the closure instant (t_c) using experimental, lubrication theory and DNS approaches.

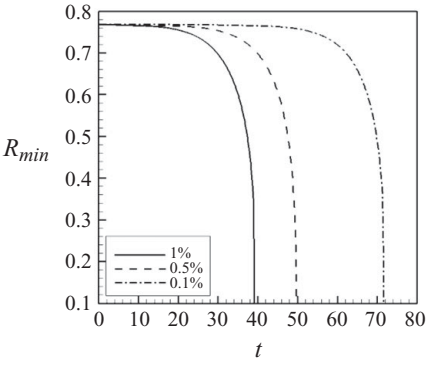


FIGURE 6. Closure histories of three different initial waves with amplitudes 0.01ε, 0.005ε and 0.001ε.

39.1 using the DNS approach and 62.8 from the experiments of Bian *et al.* (2010). The differences between the two theoretical approaches could be due to the fact that in the lubrication theory model the core is treated as a passive fluid with constant pressure, and that inertial terms and certain viscous terms are neglected.

The discrepancy in t_c between the DNS approach and the experiments may be due to uncertainties with the initial condition, the measurements of t_c and the surface tension. The initial condition used in the numerical simulations consists of a wave that has a fixed amplitude and wavelength, while in the experiments the initial condition most likely consisted of small-amplitude white noise. Figure 6 shows the influence of the initial wave amplitude on R_{min} and the closure time. For amplitudes of 0.01ε, 0.005ε and 0.001ε, the corresponding closure times are 39.1, 49.6 and 71.5, respectively. Therefore, fluctuations in the initial amplitude could account for differences in the closure time since it is not easy to discern the exact instant that the wave disturbance begins to develop in the experiments.

4.3. *Flow fields*

The flow fields for the case with $\varepsilon = 0.23$ and $L = 6.8$ are shown and compared with the experimental results (Bian *et al.* 2010) in figures 7 and 8. Because of the limitation of the camera, the image can only be shown in the range of $1.6 > z > -1.6$ in the experimental study but the actual length of the tube is $L = 6.8$ in both experimental and numerical studies. Time sequences of sample computational images before closure

https://doi.org/10.1017/jfm.2011.96 Published online by Cambridge University Press

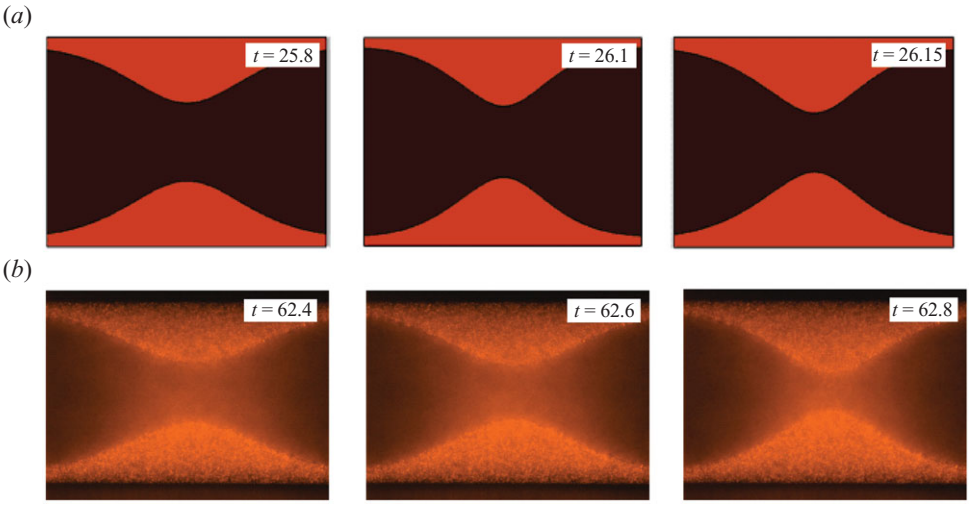


FIGURE 7. Dimensionless time sequences of the interface shape before the closure with $\varepsilon = 0.23$: (*a*) numerically computed interface position; (*b*) experimentally recorded fluorescent particle images (Bian *et al.* 2010).

are given in figure 7(*a*). It can be seen that the interface shape and location from the computed results are qualitatively consistent with those of the micro-PIV experiments in figure 7(*b*) (Bian *et al.* 2010).

Instantaneous velocity vectors, speed contours, and streamlines at two different times before closure are shown in figure 8(*a*). The experimental flow fields which are derived from three particle images are shown in figure 8(*b*) (Bian *et al.* 2010). The streamline plots from both the numerical and experimental results indicate that the liquid is driven from the edges of the film domain towards the centre. This is due to the capillary instability that induces a pressure gradient within the liquid layer and the conservation of mass within the layer. The maximum velocity is located at the bulge tip ($z = 0$) and a second velocity peak is found locally at the transition regions between the film and the bulge ($z = \pm 0.8$). The streamlines are approximately perpendicular to the surface of the tip area, while a vortical structure is observed near the interface between the tip and the transition areas ($1.6 > z > -1.6$), consistent with the numerical results of Campana *et al.* (2004). Close-up views of the velocity vectors near the bulge tip at the instant before closure from the numerical simulation and the experiment are shown in figure 8(*c*), respectively. The vectors are found to point outwardly from the centre of the tip, indicating that the interface is being stretched horizontally and vertically at the same time before closure.

4.4. *Wall shear stresses*

The numerically computed shear stress along the inner wall of the airway $\tau_w^* = -\mu^*(\partial w^*/\partial z^*)|_{r^*=a^*}$ at different time steps is plotted in figure 9(*a*). It shows that the shear stress increases as the interface deforms. The maximum shear stress magnitudes occur at $z = \pm 0.8$ at the last computational time step. As time increases, the stress magnitudes increase and become large near the end of the closure process when velocities are high. When $t = 26.24$ ($t^* = 0.88$ s), the shear stress maxima are ± 80 dyn cm^{-2}, which is in the range of stress levels that damage airway epithelial cells reported during the reopening process (Bilek *et al.* 2003; Huh *et al.* 2007). In figure 9(*b*), the wall shear stress is scaled by the maximum wall stress value at the

https://doi.org/10.1017/jfm.2011.96 Published online by Cambridge University Press

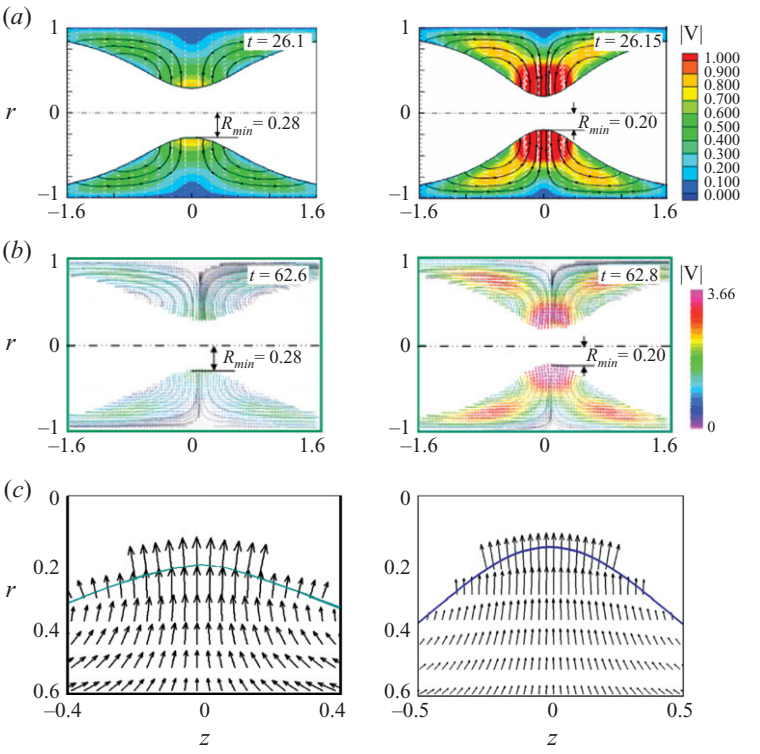


FIGURE 8. Dimensionless velocity fields, speed contours and streamlines in the liquid layer for $\varepsilon = 0.23$ before the closure: (*a*) numerical results and (*b*) experimental results (Bian *et al.* 2010). A close-up of the velocity vector near the bulge tip is also given. (*c*) Experimental data at $t = 62.8$ (Bian *et al.* 2010) and numerical data at $t = 26.15$.

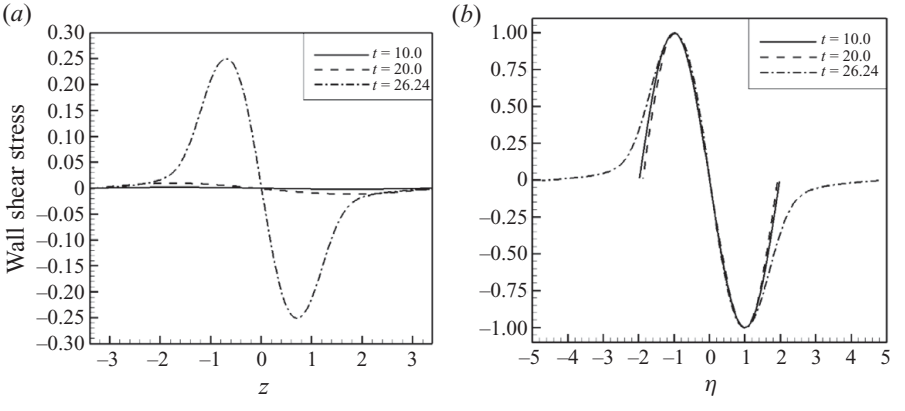


FIGURE 9. Profiles of the wall shear stress along on the inner surface of the airway at various times before closure with $\varepsilon = 0.23$: (*a*) results scaled by σ^*/a^*; (*b*) results scaled by the maximum shear stress and plotted against $\eta = z/z_{max}$.

given time. The dimensionless parameter η is defined as z/z_{max}, where z_{max} is the axial location of the maximum wall shear stress at each instant. It can be seen that nearly all of the wall shear stress data collapse into one single sinusoidal curve before

https://doi.org/10.1017/jfm.2011.96 Published online by Cambridge University Press

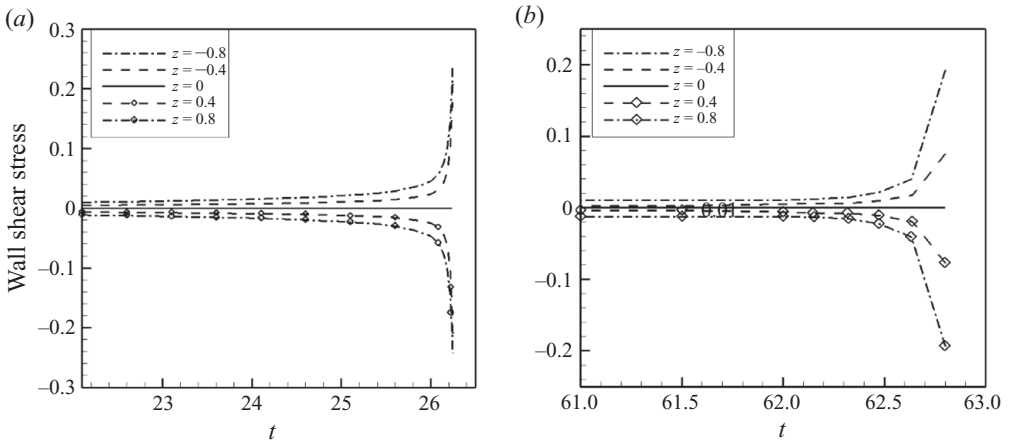


FIGURE 10. Time history of the wall shear stress scaled by σ^*/a^* at various axial locations with $\varepsilon = 0.23$: (*a*) numerical results and (*b*) experimental data (Bian *et al.* 2010).

closure, indicating that the film growth is dominated by linear instability until the very last instants when the evolution of the film starts to be influenced by nonlinear effects. Also, the location of the maximum wall shear stress moves towards the bulge ($z = 0$) as $t \to t_c$, which is consistent with the presence of the local velocity peaks seen in figure 8(*c*).

The evolution of the wall shear stress versus time at various axial locations is shown in figure 10.

Both the numerical and the experimental results show that the wall shear stress increases gradually and then accelerates rapidly when closure is about to occur. Also, both approaches confirm that the wall shear stress increases significantly at closure. In the airway, the epithelial cells not only experience a high shear stress but also a large spatial gradient and a dramatic temporal fluctuation, both of which might be injurious to the cells.

4.5. *Pressure fields and wall-normal stresses*

The numerically computed speed, streamlines and pressure contours for different times with $\varepsilon = 0.23$ are shown in figure 11. Initially, the perturbation is small, and consequently the interface deforms slowly and the generated velocity in the liquid layer is small. As the deformation becomes larger, the interfacial curvature also increases, inducing larger flows and deformations. The locations of maximum speed change are initially located at the transition regions. As $t \to t_c$, these locations move towards the tip of the bulge. The locations of maximum pressure are approximately at $z = \pm 2.2$, when the deformation is small. The maximum speed locations are approximately at $z = +2$ and -2 at early times. With time, these locations move towards the centre and eventually merge. In this model for $\varepsilon = 0.23$, the pressure in the gas phase is set to a constant value $p_g = \kappa/\varepsilon = 5.65$. Therefore, the pressure in the liquid film is initially negative in order to satisfy the normal stress condition at the interface. At early times, when the deformation is small, the pressure contours are essentially vertical straight lines, indicating that the pressure distribution is only a function of the axial location and time, that is $p = p(z, t)$ (figures 11*a* and 11*b*). However, once the deformation is large enough (figure 11*c*), the pressure develops a strong radial dependence (which the lubrication theory model fails to capture), and has a strong negative value near the bulge tip which is needed to balance the surface tension.

https://doi.org/10.1017/jfm.2011.96 Published online by Cambridge University Press

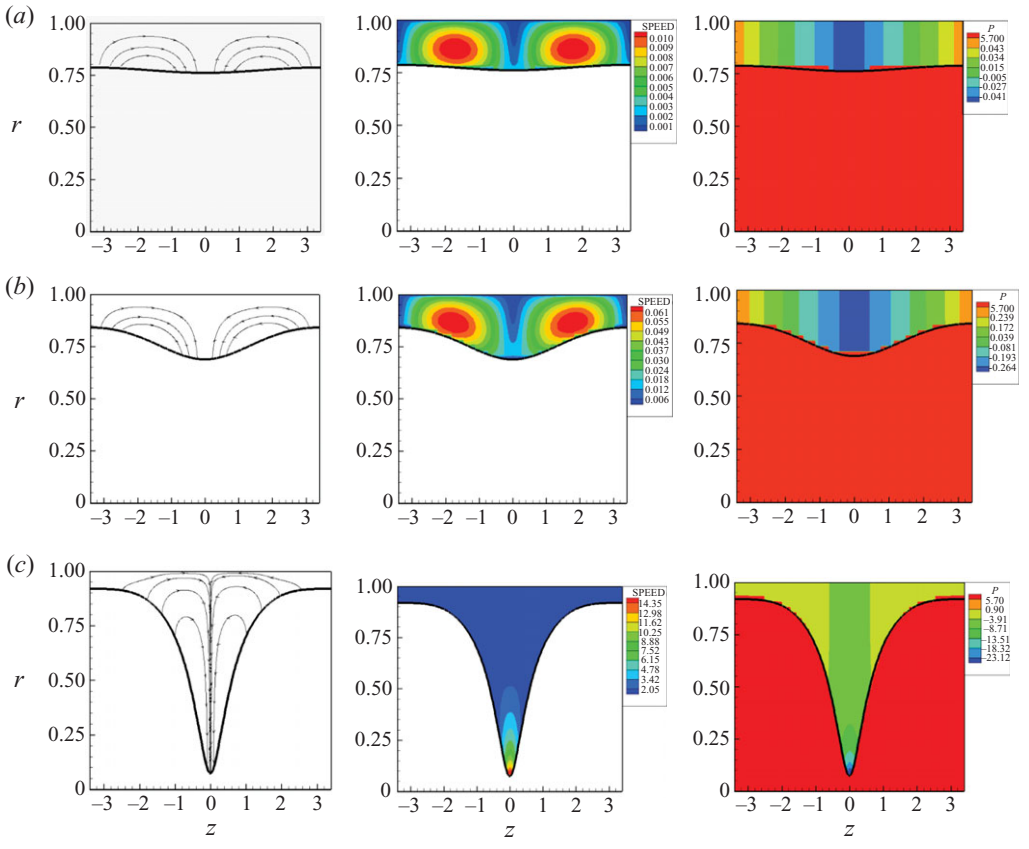


FIGURE 11. Streamlines, speed contours and pressure contours scaled by $\varepsilon\sigma^*/a^*$ for $\varepsilon = 0.23$ at various time steps: (*a*) $t = 10.0$, (*b*) $t = 20.0$ and (*c*) $t = 26.24$.

Figure 12(*a*) shows the numerically computed dimensionless normal stresses on the inner wall of the airway $\sigma_w^* = -p_f^*|_{r^*=a^*}$ at different time steps. This can be easily computed using the DNS approach. In the experimental approach such as micro-PIV, the velocities can be measured but it is much more difficult to measure pressure accurately.

Figure 12 shows that the normal wall stresses increase as the interface deforms and the maximum magnitude of the normal stress, which is 410 dyn cm^{-2}, is much larger than the maximum shear stress in figure 9, which is about ± 80 dyn cm^{-2}. The maximum normal stress on the wall occurs at the centre of the growing liquid bulge, $z = 0$. As time increases, the stress magnitudes increase and become large near the end of the closure process when velocities are high. Figure 12(*b*) shows that the maximum wall-normal stress increases gradually with time when the disturbance grows exponentially ($t < 20$). When the growth of the disturbance is strongly affected by nonlinear effects near the closure time ($t \geqslant 20$), the maximum wall-normal stress increases abruptly.

Spatial gradients of the computed wall-normal and shear stresses at $t = 26.24$ ($t^* = 0.88$ s) are shown in figure 13. The maximum wall-normal stress gradient is located at $z = \pm 0.8$, approximately where the maximum and minimum wall shear stresses exist. The wall shear stress gradient has a peak at $z = 0$, where the wall shear

https://doi.org/10.1017/jfm.2011.96 Published online by Cambridge University Press

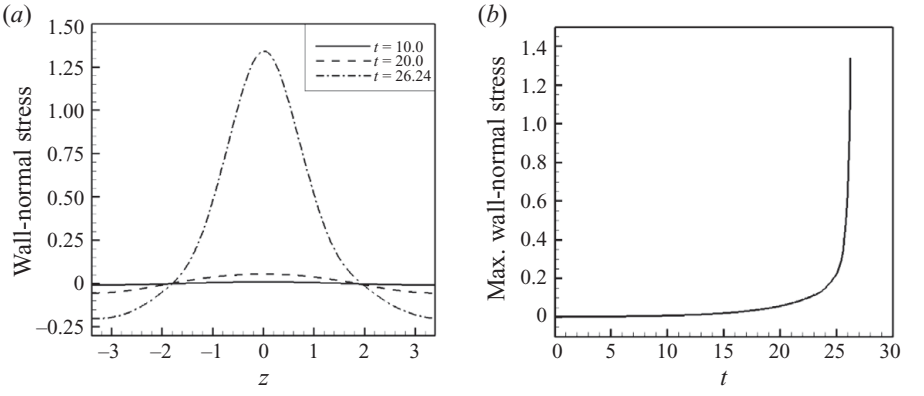


FIGURE 12. (*a*) Normal stress scaled by σ^*/a^* along on the inner surface of the airway at various time instants with $\varepsilon = 0.23$. (*b*) Maximum normal stress on the inner surface of the airway versus time.

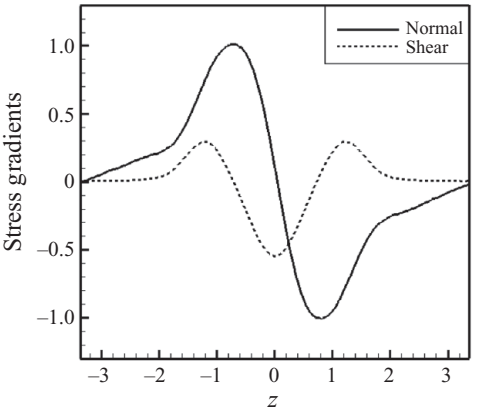


FIGURE 13. Spatial gradients of the normal and shear stresses at $t = 26.24$.

stress changes signs and the maximum wall-normal stress is. Two positive peaks for the wall shear stress are found near $z = \pm 1.2$. The magnitude of the maximum wall-normal stress gradient is approximately 3–4 times higher than that of the maximum wall shear stress gradient as discussed above.

4.6. *Impact of film thickness on the wall stresses*

In order to compare the numerical and experimental results, most results shown in the previous sections are for $\varepsilon = 0.23$. In this section, the impact of the film thickness on the wall stresses is investigated. Figure 14 shows R_{min} as a function of a dimensionless time $t^*/(\mu_f^* a^*/\sigma^*)$ which is independent of ε for $\varepsilon = 0.19, 0.23, 0.27$. This figure clearly demonstrates that R_{min} decreases more quickly with increasing ε and that the closure time decreases with increasing ε.

Normal and shear stresses along the tube wall for different values of ε are shown in figures 15 and 16. The stresses are scaled with respect to σ^*/a^*. Figure 15 shows the shear and normal stresses for $\varepsilon = 0.19$, 0.23 and 0.27, when R_{min} reaches 0.3. In all three cases, both stresses are higher for the case with $\varepsilon = 0.27$. In figure 15(*a*), the

https://doi.org/10.1017/jfm.2011.96 Published online by Cambridge University Press

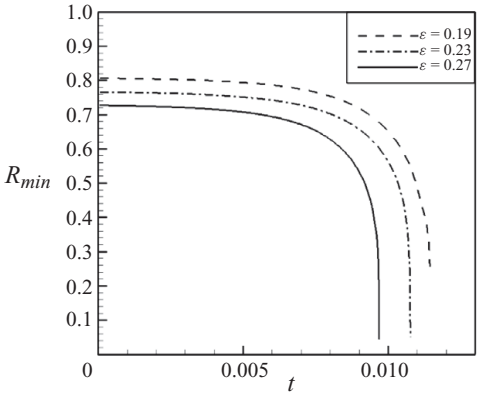


FIGURE 14. The minimum core radius as a function of time for $\varepsilon = 0.19$, 0.23 and 0.27.

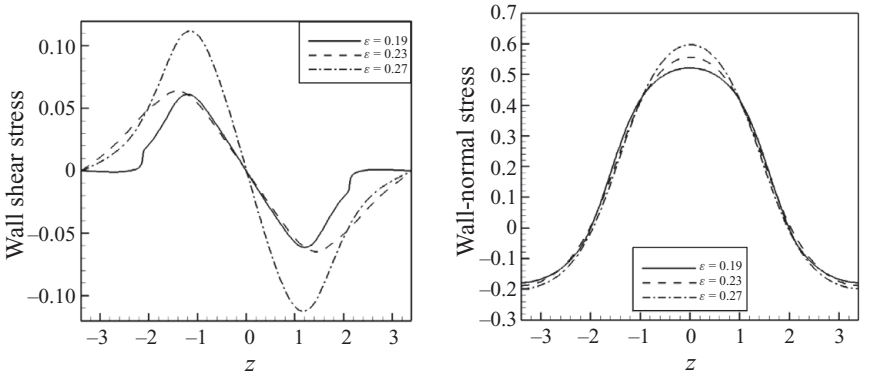


FIGURE 15. (*a*) Shear and (*b*) normal stresses scaled by σ^*/a^* on the inner surface of the airway along the axial direction when $R_{min} = 0.3$ for $\varepsilon = 0.19$, 0.23 and 0.27.

maximum shear stress is similar for $\varepsilon = 0.19$ and 0.23 but the shear stress decays faster for the case with $\varepsilon = 0.19$ when $z > 2$ and $z < -2$. For the case where $\varepsilon = 0.19$, the shape of the interface is flatter when $z > 2$ and $z < -2$. In figure 15(*b*), the interfacial velocity decreases in this area due to the increased resistance from the wall as the interface deforms. Once the interfacial velocity decreases, the induced liquid flow decreases and results in a decrease in the normal stress.

4.7. *Self-similar behaviour near the closure event*

Since R^*_{min} approaches zero when closure occurs, the solution in the neighbourhood of where this happens does not have a characteristic length scale. So, presumably a similarity solution exists that describes the closure event. In the breakup of a liquid bridge between two plates (Keller & Miksis 1983; Chen & Steen 1997; Eggers 1997), there is a 2/3-power-law relation between the diameter of the liquid bridge and the time to breakup, $(t^*_c - t^*)$, $d^* = (\sigma^*(t^*_c - t^*)^2/\rho^*)^{1/3}$, where d^* is the diameter of the liquid bridge. In figure 16(*a*), R^*_{min} is plotted as a function of $(t^*_c - t^*)$ using a log–log scale with $\varepsilon = 0.23$. There are two distinct regimes. At the beginning of closure, the slope of the curve is approximately 0.175, while near the pinch-off the slope is about 0.5. The differences in these slopes may be attributed to different forces that play dominant roles at different times. The review paper by Eggers & Villermaux (2008) discusses the possible scaling regimes during the breakup of liquid bridges. The

https://doi.org/10.1017/jfm.2011.96 Published online by Cambridge University Press

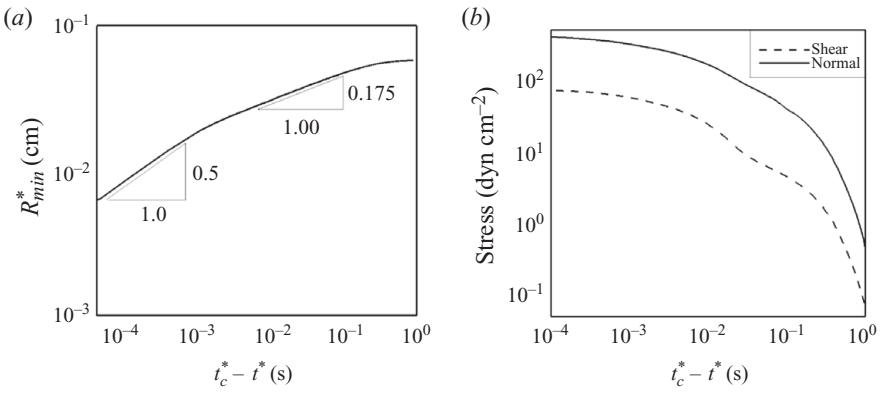


FIGURE 16. The log–log plots of the (*a*) R^*_{min} and (*b*) maximal wall stresses versus $(t^*_c - t^*)$ for $\varepsilon = 0.23$.

smaller slope of 0.175 can occur when the dominant effects are due to surface tension and viscosity alone, while the larger slope of 0.5 suggests that there is a balance between surface tension, inertia and viscous effects. The 2/3-power-law mentioned above is based on a dominant balance between fluid inertia and surface tension, and does not include viscous effects that are important in the closure problem. In the airway closure model, the distance between the interface and the surface of the tube can be very small, and thus the effect of film viscosity cannot be ignored. In figure 11(*b*), one can see that during the early stages of the airway closure ($t < 20$), the system is almost quiescent, and the induced velocities are very small. The maximum speed is only about 0.061, and it can be expected that the effects of inertia should be weak. Hence, there is a balance between viscous and surface tension effects. As the interface deforms, the velocities in the layers increase rapidly. In figure 11(*c*), the maximum speed can reach 14.35, while the minimum speed is still around zero. This means that the induced speed and its spatial gradient are much larger compared with those shown in figure 11(*b*). The maximum speed increases more than 235 times from $t = 20$ to 26.24. Consequently, near the closure event, inertia should not be neglected. In contrast, the maximum shear stress only increases 25 times compared with that shown in figure 9(*a*). We can therefore infer that at some point, there is a balance between viscous, inertia and surface tension effects. This occurs near the pinch-off.

In figure 16(*b*), we plot the maximum shear and normal stresses as well as functions of $(t^*_c - t^*)$ in a log–log scale. As with R^*_{min}, there are two distinct slopes. When $(t^*_c - t^*) \to 0$, the slopes are fairly small but still negative, indicating that the maximum wall stresses grow without bound in this airway closure model. These results are also confirmed by figures 10(*a*) and 12(*b*).

5. Conclusions

The liquid lining in small human airways is unstable and can form liquid plugs that close off the airways. Instead of the simplified lubrication theory approach, the DNS in which the full set of governing equations is solved has been performed in an airway model to study the airway instability and the flow-induced stresses on the airway walls. The DNS approach can offer an accurate value of the primary flow variables and the location of the free interface at different time steps.

https://doi.org/10.1017/jfm.2011.96 Published online by Cambridge University Press

A thin annular film lining the inside of a rigid tube is modelled as a liquid-lined airway in the numerical simulations. The dynamics of the closure process is simulated for a Newtonian viscous film with constant surface tension and a passive core gas phase. The computed flow fields and stress distributions are consistent with those acquired in the experiments. The numerical results are compared with the experimental data (Bian *et al.* 2010) and the comparison is favourable.

Instantaneous velocity fields in the annular film at various stages of the airway closure show multiple local velocity peaks located at the bulge tip and the transition region. The wall stresses at the time instant of closure is one order of magnitude larger than that before the closure, indicating a large stress spatial gradient and temporal gradient on the airway wall. One can see that both normal and shear stresses increase with time in the airway closure model, and both have high values near the end of closure (at $t = 26.24$, $t^* = 0.88$ s) due to the large induced velocity in the liquid film and large variations of interfacial curvature.

The greatest damage to the cells occurs at the end of the closure under the conditions just described. In contrast, in the reopening model (Bilek *et al.* 2003), cell damage increases with decreasing reopening velocity. Bilek *et al.* (2003) found that as the reopening velocity decreases, the thickness of the trailing film decreases, and there is a tremendous increase in the pressure difference in the transition region. Since the size of a typical cell is very small (40 μm), the pressure difference over such a cell may be very large, resulting in large cell deformation and leading to cell injury or even death. However, there are also scenarios where the surface stresses can deform cells and induce injury. In the experiments of Bilek *et al.*, cell damage can occur when $(\tau_s)_{max} > 12.9\,\mathrm{dyn\,cm^{-2}}$, $(\mathrm{d}\tau_s/\mathrm{d}x)_{max} > 2.1 \times 10^3\,\mathrm{dyn\,cm^{-3}}$ and $(\mathrm{d}p/\mathrm{d}x)_{max} > 3.21 \times 10^4\,\mathrm{dyn\,cm^{-3}}$. Huh *et al.* (2007) reported that cells are damaged when $(\tau_s)_{max} > 97.58\,\mathrm{dyn\,cm^{-2}}$ and $(p)_{max} > 6.4 \times 10^3\,\mathrm{dyn\,cm^{-2}}$. In the current airway closure model, the corresponding quantities with $\varepsilon = 0.23$ are $(\tau_s)_{max}$ $80\,\mathrm{dyn\,cm^{-2}}$, $(p)_{max}$ $410\,\mathrm{dyn\,cm^{-2}}$, $(\mathrm{d}\tau_s/\mathrm{d}x)_{max}$ $1.48 \times 10^3\,\mathrm{dyn\,cm^{-3}}$ and $(\mathrm{d}p/\mathrm{d}x)_{max}$ $4.82 \times 10^3\,\mathrm{dyn\,cm^{-3}}$. The shear stress is larger but the pressure and the gradients are smaller than those in the experiments. It should be noted that the above quantities are based on the current selected parameters. It is expected that as ε decreases, the stresses may increase further.

The computational results also show that the wall shear stress, normal stress and their gradients during closure can be high enough to injure airway epithelial cells. These findings are consistent with the conclusions of the experimental study by Bian *et al.* (2010).

We also performed a self-similar analysis during the closure event. The minimum core radius, R^*_{min}, was found to be approximately proportional to $(t^*_c - t^*)^{0.175}$ at the beginning of the closure event, implying a balance between viscous and surface tension effects. Later, near the pinch-off event, inertia also becomes important, and $R^*_{min} \propto (t^*_c - t^*)^{0.5}$. Both of these exponents suggest that viscous effects play a significant role in the airway closure model.

We thank Dr Benjamin Vaughan for his insightful comments on this manuscript. This work is supported by NIH grants HL85156 and HL84370.

REFERENCES

Baker, C. S., Evans, T. W., Randle, B. J. & Haslam, P. L. 1999 Damage to surfactant-specific protein in acute respiratory distress syndrome. *Lancet* **353**, 1232–1237.

https://doi.org/10.1017/jfm.2011.96 Published online by Cambridge University Press

Bian, S., Tai, C.-F., Halpern, D., Zheng, Y. & Grotberg, J. B. 2010 Experimental study of flow fields in an airway closure model. *J. Fluid Mech.* **647**, 391–402.

Bilek, A. M., Dee, K. C. & Gaver, D. P. 2003 Mechanisms of surface-tension-induced epithelial cell damage in a model of pulmonary airway reopening. *J. Appl. Physiol.* **94**, 770–783.

Campana, D. M., Di Paolo, J. & Saita, F. A. 2004 A 2-D model of Rayleigh instability in capillary tubes – surfactant effects. *Intl J. Multiphase Flow* **30**, 431–454.

Campana, D. M. & Saita, F. A. 2006 Numerical analysis of the Rayleigh instability in capillary tubes: The influence of surfactant solubility. *Phys. Fluids* **18**, 022104.

Cassidy, K. J., Halpern, D., Ressler, B. G. & Grotberg, J. B. 1999 Surfactant effects in model airway closure experiments. *J. Appl. Physiol.* **87**, 415–427.

Chen, Y. J. & Steen, P. H. 1997 Dynamics of inviscid capillary breakup: collapse and pinchoff of a film bridge. *J. Fluid Mech.* **341**, 245–267.

Crystal, R. G. 1997 *The Lung: Scientific Foundations*. Lippincott.

Dargaville, P. A., South, M. & McDougall, P. N. 1996 Surfactant abnormalities in infants with severe viral bronchiolitis. *Arch. Dis. Child.* **75**, 133–136.

Eggers, J. 1997 Nonlinear dynamics and breakup of free-surface flows. *Rev. Mod. Phys.* **69**, 865–929.

Eggers, J. & Villermaux, E. 2008 Physics of liquid jets. *Rep. Prog. Phys.* **71**, 036601.

Ferziger, J. H. & Peric, M. 1996 *Computational Methods for Fluid Dynamics*. Springer.

Fujioka, H. & Grotberg, J. B. 2004 Steady propagation of a liquid plug in a two-dimensional channel. *J. Biomech. Engng - Trans. ASME* **126**, 567–577.

Fujioka, H. & Grotberg, J. B. 2005 The steady propagation of a surfactant-laden liquid plug in a two-dimensional channel. *Phys. Fluids* **17**, 082102.

Fujioka, H., Takayama, S. & Grotberg, J. B. 2008 Unsteady propagation of a liquid plug in a liquid-lined straight tube. *Phys. Fluids* **20**, 062104.

Ghadiali, S. N. & Gaver, D. P. 2008 Biomechanics of liquid–epithelium interactions in pulmonary airways. *Respir. Physiol. Neurobiol.* **163**, 232–243.

Greaves, I. A., Hildebrandt, J. & Hoppin, J. F. G. 1986 *Handbook of Physiology. The Respiratory System: Mechanics of Breathing*. American Physiology Society.

Griese, M., Essl, R., Schmidt, R., Rietschel, E., Ratjen, F., Ballmann, M. & Paul, K. 2004 Pulmonary surfactant, lung function, and endobronchial inflammation in cystic fibrosis. *Am. J. Respir. Crit. Care Med.* **170**, 1000–1005.

Guerin, C., LeMasson, S., DeVarax, R., MilicEmili, J. & Fournier, G. 1997 Small airway closure and positive end-expiratory pressure in mechanically ventilated patients with chronic obstructive pulmonary disease. *Am. J. Respir. Crit. Care Med.* **155**, 1949–1956.

Gunther, A., Siebert, C., Schmidt, R., Ziegler, S., Grimminger, F., Yabut, M., Temmesfeld, B., Walmrath, D., Morr, H. & Seeger, W. 1996 Surfactant alterations in severe pneumonia, acute respiratory distress syndrome, and cardiogenic lung edema. *Am. J. Respir. Crit. Care Med.* **153**, 176–184.

Halpern, D., Fujioka, H. & Grotberg, J. B. 2010 The effect of viscoelasticity on the stability of a pulmonary airway liquid layer. *Phys. Fluids* **22**, 011901.

Halpern, D. & Grotberg, J. B. 1992 Fluid-elastic instabilities of liquid-lined flexible tubes. *J. Fluid Mech.* **244**, 615–632.

Halpern, D. & Grotberg, J. B. 1993 Surfactant effects on fluid-elastic instabilities of liquid-lined flexible tubes: a model of airway closure. *J. Biomech. Engng - Trans. ASME* **115**, 271–277.

Halpern, D. & Grotberg, J. B. 2003 Nonlinear saturation of the Rayleigh instability due to oscillatory flow in a liquid-lined tube. *J. Fluid Mech.* **492**, 251–270.

Hammond, P. S. 1983 Nonlinear adjustment of a thin annular film of viscous-fluid surrounding a thread of another within a circular cylindrical pipe. *J. Fluid Mech.* **137**, 363–384.

Heil, M. 1999 Airway closure: Occluding liquid bridges in strongly buckled elastic tubes. *J. Biomech. Engng - Trans. ASME* **121**, 487–493.

Heil, M., Hazel, A. L. & Smith, J. A. 2008 The mechanics of airway closure. *Respir. Physiol. Neurobiol.* **163**, 214–221.

Hirt, C. W. & Nichols, B. D. 1981 Volume of fluid (VOF) method for the dynamics of free boundaries. *J. Comput. Phys.* **39**, 201–225.

Huh, D., Fujioka, H., Tung, Y. C., Futai, N., Paine, R., Grotberg, J. B. & Takayama, S. 2007 Acoustically detectable cellular-level lung injury induced by fluid mechanical stresses in microfluidic airway systems. *Proc. Natl Acad. Sci. USA* **104**, 18886–18891.

https://doi.org/10.1017/jfm.2011.96 Published online by Cambridge University Press

Johnson, M., Kamm, R. D., Ho, L. W., Shapiro, A. & Pedley, T. J. 1991 The nonlinear growth of surface-tension-driven instabilities of a thin annular film. *J. Fluid Mech.* **233**, 141–156.

Kay, S. S., Bilek, A. M., Dee, K. C. & Gaver, D. P. 2004 Pressure gradient, not exposure duration, determines the extent of epithelial cell damage in a model of pulmonary airway reopening. *J. Appl. Physiol.* **97**, 269–276.

Keller, J. B. & Miksis, M. J. 1983 Surface-tension-driven flows. *SIAM J. Appl. Math.* **43**, 268–277.

Macklem, P. T., Proctor, D. F. & Hogg, J. C. 1970 Stability of peripheral airways. *Respir. Physiol.* **8**, 191–203.

Muscedere, J. G., Mullen, J. B. M., Gan, K. & Slutsky, A. S. 1994 Tidal ventilation at low airway pressures can augment lung injury. *Am. J. Respir. Crit. Care Med.* **149**, 1327–1334.

Osher, S. J. & Fedkiw, R. P. 2003 *Level Set Methods and Dynamic Implicit Surfaces*. Springer.

Peskin, C. S. 1977 Numerical analysis of blood flow in the heart. *J. Comput. Phys.* **25**, 220–252.

Piirila, P. & Sovijarvi, A. R. A. 1995 Crackles: recording, analysis and clinical significance. *Eur. Respir. J.* **8**, 2139–2148.

Rasanen, J. & Gavriely, N. 2005 Response of acoustic transmission to positive airway pressure therapy in experimental lung injury. *Intensive Care Med.* **31**, 1434–1441.

Ryskin, G. & Leal, L. G. 1984 Numerical solution of free-boundary problems in fluid mechanics. Part 2. Buoyancy-driven motion of a gas bubble through a quiescent liquid. *J. Fluid Mech.* **148**, 19–35.

Shyy, W. 1994 *Computational Modeling for Fluid Flow and Interfacial Transport*. Elsevier.

Tai, C.-F. & Shyy, W. 2005 Multigrid computations and conservation law treatment of a sharp interface method. *Numer. Heat Trans.* B **48**, 405–424.

Taskar, V., John, J., Evander, E., Robertson, B. & Jonson, B. 1997 Surfactant dysfunction makes lungs vulnerable to repetitive collapse and reexpansion. *Am. J. Respir. Crit. Care Med.* **155**, 313–320.

t Veen, J., Beekman, A. J., Bel, E. H. & Sterk, P. J. 2000 Recurrent exacerbations in severe asthma are associated with enhanced airway closure during stable episodes. *Am. J. Respir. Crit. Care Med.* **161**, 1902–1906.

White, J. P. & Heil, M. 2005 Three-dimensional instabilities of liquid-lined elastic tubes: A thin-film fluid–structure interaction model. *Phys. Fluids* **17**, 031506.

Ye, T., Shyy, W., Tai, C.-F. & Chung, J. 2004 Assessment of sharp- and continuous-interface methods for drop in static equilibrium. *Comput. Fluids* **33**, 917–926.

Zheng, Y., Fujioka, H., Bian, S., Torisawa, Y., Huh, D., Takayama, S. & Grotberg, J. B. 2009 Liquid plug propagation in flexible microchannels – a small airway model. *Phys. Fluids* **21**, 071903.

https://doi.org/10.1017/jfm.2011.96 Published online by Cambridge University Press